

Numerical studies on the linear and nonlinear evolutions of infernal modes

Jiu-Ying Li(李久瑛), Wei Zhang(张威), Zi-Xi Liu(刘子奚), Zhi-Wei Ma(马志为), Fei-Fei Long(龙飞飞), Cheng-Cheng Deng(邓成成), Peng-Cheng Li(厉鹏程), Kang-Ning Yang(杨康宁), Xiao-Yu Yin(尹晓宇), Run-Zhi Hu(胡润志), Yi-An Zhao(赵一安), Hong Li(李弘), Jin-Lin Xie(谢锦林), Tao Lan(兰涛), Wen-Zhe Mao(毛文哲), A-Di Liu(刘阿娣), Chu Zhou(周楚), Wei-Xing Ding(丁卫星), Ge Zhuang(庄革), and Wan-Dong Liu(刘万东)
Citation: Chin. Phys. B, 2026, 35 (**7**): 075201. DOI: 10.1088/1674-1056/ae1016
http://cpb.iphy.ac.cn; http://iopscience.iop.org/cpb

What follows is a list of articles you may be interested in

Effects of diamagnetic drift on nonlinear interaction between multi-helicity neoclassical tearing modes

Haiyuan Wang(王海源), Shuai Jiang(姜帅), Tong Liu(刘桐), Lai Wei(魏来), Qibin Luan(栾其斌), and Zheng-Xiong Wang(王正汹)
Chin. Phys. B, 2024, 33 (**6**): 065202. DOI: 10.1088/1674-1056/ad24d3

Error field penetration in J-TEXT tokamak based on two-fluid drift-MHD model

Wen Wang(王文), Tao Xu(徐涛), Yi Zhang(张仪), and the J-TEXT team
Chin. Phys. B, 2024, 33 (**4**): 045202. DOI: 10.1088/1674-1056/ad1e6b

Effects of plasma radiation on the nonlinear evolution of neo-classical tearing modes in tokamak plasmas with reversed magnetic shear

Shuai Jiang(姜帅), Zheng-Xiong Wang(王正汹), Lai Wei(魏来), and Tong Liu(刘桐)
Chin. Phys. B, 2023, 32 (**10**): 105203. DOI: 10.1088/1674-1056/acedf7

Linear analysis of plasma pressure-driven mode in reversed shear cylindrical tokamak plasmas

Ding-Zong Zhang(张定宗), Xu-Ming Feng(冯旭铭), Jun Ma(马骏), Wen-Feng Guo(郭文峰), Yan-Qing Huang(黄艳清), and Hong-Bo Liu(刘洪波)
Chin. Phys. B, 2023, 32 (**1**): 015201. DOI: 10.1088/1674-1056/ac70b4

Scaling of rise time of drive current on development of magneto-Rayleigh-Taylor instabilities for single-shell Z-pinches

Xiaoguang Wang(王小光), Guanqiong Wang(王冠琼), Shunkai Sun(孙顺凯), Delong Xiao(肖德龙), Ning Ding(丁宁), Chongyang Mao(毛重阳), and Xiaojian Shu(束小建)
Chin. Phys. B, 2022, 31 (**2**): 025203. DOI: 10.1088/1674-1056/ac1fd9

Numerical studies on the linear and nonlinear evolutions of infernal modes

Jiu-Ying Li(李久瑛)[1], Wei Zhang(张威)[2,†], Zi-Xi Liu(刘子奚)[1,‡], Zhi-Wei Ma(马志为)[2], Fei-Fei Long(龙飞飞)[1], Cheng-Cheng Deng(邓成成)[1], Peng-Cheng Li(厉鹏程)[1], Kang-Ning Yang(杨康宁)[1], Xiao-Yu Yin(尹晓宇)[1], Run-Zhi Hu(胡润志)[1], Yi-An Zhao(赵一安)[1], Hong Li(李弘)[1], Jin-Lin Xie(谢锦林)[1], Tao Lan(兰涛)[1], Wen-Zhe Mao(毛文哲)[1], A-Di Liu(刘阿娣)[1], Chu Zhou(周楚)[1], Wei-Xing Ding(丁卫星)[1], Ge Zhuang(庄革)[1], and Wan-Dong Liu(刘万东)[1]

[1] *Department of Plasma Physics and Fusion Engineering, University of Science and Technology of China, Hefei* 230026, *China*
[2] *Institute for Fusion Theory and Simulation, School of Physics, Zhejiang University, Hangzhou* 310027, *China*

(Received 7 July 2025; revised manuscript received 25 September 2025; accepted manuscript online 7 October 2025)

The present paper numerically investigates the linear and nonlinear evolution of infernal modes through a three-dimensional, toroidal geometric, nonlinear, and full-MHD code CLT. For equilibria with $q_{\min} \approx 2.0$, the development of the infernal modes leads to an elongated high-pressure region. We find that the nonlinear behaviors of the infernal modes can be totally different when the parallel thermal conductivity exceeds a threshold. Below this threshold, the infernal modes experience explosive growth in the nonlinear stage; above this threshold, they finally saturate in the nonlinear phase. For the cases with nonlinearly explosive growth, the patterns of the perturbed pressure are 'ballooning-like' and the dominant modes are with $n > 1$, where n is the toroidal mode number. When the parallel thermal conductivity exceeds the threshold, the parallel diffusion along the magnetic field lines is quick enough. Then the nonlinearly explosive growth is suppressed, and the infernal modes will saturate in the nonlinear stage. A two-dimensional (2D) parameter map is provided to illustrate the transition between these distinct nonlinear regimes.

Keywords: infernal mode, long-live mode, pressure driven, explosive growth

PACS: 52.30.Cv, 52.65.–y, 52.35.Mw, 52.55.Tn

DOI: 10.1088/1674-1056/ae1016 **CSTR:** 32038.14.CPB.ae1016

1. Introduction

The hybrid tokamak scenarios, characterized by weakly reversed or nearly flat safety factor profiles, offer substantial potential for steady-state operation with high confinement and high beta.[1,2] Due to the absence of $q = 1$ rational surfaces, these hybrid scenarios can avoid phenomena that degrade performance, such as sawteeth[3] and sawtooth-triggered neoclassical tearing modes (NTMs).[4–6] However, near a rational surface, the combination of a strong pressure gradient and weak shear gives rise to pressure-driven modes: the quasi-interchange mode[7–11] (for $q_{\min} \approx 1$) or the infernal modes[12–14] (for $q_{\min} > 1$), both of which can be triggered even if there are no exact resonant surfaces. In many tokamaks, they are sometimes referred to as long-lived modes (LLMs), *e.g.*, in JET,[15,16] NSTX,[17,18] MAST,[19] HL-2A,[20–25] LHD,[26] ASDEX Upgrade,[27] and EAST.[28,29] Such instabilities are particularly dangerous and can lead to major disruptions.[30,31] As a result, the analysis, threshold identification, and control of these instabilities remain active and critical areas of research.[14,32–36]

Infernal modes are defined as the coupling between a (m, n) mode and its poloidal sidebands ($m \pm 1$, n). Here, m and n are the poloidal and toroidal mode numbers, respectively. The coupling between them is associated with toroidal effects, resulting in a dispersion relation that is distinct from that of typical tearing modes in low-shear regions.[37,38] This difference leads to a variety of resistive scalings that depend on plasma pressure. Far below the threshold of the ideal instability, the mode's growth rate exhibits a tearing-like scaling law, *i.e.*, $\gamma \sim \eta^{3/5}$, where η is the plasma resistivity. When the plasma pressure increases to the threshold of the ideal instability, the scaling law changes to $\gamma \sim \eta^{3/13}$.[39] With further increases in plasma pressure, the mode becomes almost independent of resistivity, *i.e.*, $\gamma \sim \eta^{0}$. Additionally, when considering sheared toroidal flow and viscosity near the ideal ion-diamagnetic magneto-hydrodynamic stability boundary, the scaling law transitions to $\eta^{3/8}$.[40] For reversed-shear equilibria, interchange theory predicts that the scaling law will be $\gamma \sim \eta^{1/3}$.[41]

Electron cyclotron emission (ECE) data can clearly identify that such disruptions are caused by nonlinear evolution of the infernal modes.[42,43] Significant progress has been made in understanding these phenomena through various stud-

†Corresponding author. E-mail: wzhang_ifts@zju.edu.cn
‡Corresponding author. E-mail: zxliu316@ustc.edu.cn

© 2026 Chinese Physical Society and IOP Publishing Ltd. All rights, including for text and data mining, AI training, and similar technologies, are reserved.

ies. In certain cases, infernal modes saturate into LLMs during the nonlinear phase.[19,20] Lütjens and Luciani demonstrated that $n = 1$ internal kink-driven ballooning modes can experience nonlinear destabilization without entering an explosive phase.[44] However, a study by Myers *et al*., studying ballooning modes near marginal stability, which investigates ballooning modes near marginal stability, reports an explosive phase that appears to terminate in a finite-time singularity, suggesting that under certain conditions, the system may evolve into a truly explosive regime.[45] Despite these advancements, the nonlinear evolution of infernal modes remains incompletely understood. This paper presents a numerical investigation of the evolution of infernal modes, especially for the explosive growth in the nonlinear stage.

2. Numerical model

CLT is an initial value resistive-MHD code with the toroidal geometry used to study MHD instabilities in magnetically confined fusion devices.[46] The complete set of resistive MHD equations used in the CLT code is given as follows:

$$\frac{\partial \rho}{\partial t} = -\nabla\cdot(\rho \boldsymbol{v}) + \nabla\cdot\left[D\nabla(\rho-\rho_0)\right], \tag{1}$$

$$\frac{\partial p}{\partial t} = -\boldsymbol{v}\cdot\nabla p - \Gamma p\nabla\cdot\boldsymbol{v} + \nabla\cdot\left[\kappa_\perp\nabla(p-p_0)\right] + \nabla\cdot\left[\kappa_\parallel\nabla_\parallel p\right], \tag{2}$$

$$\frac{\partial \boldsymbol{v}}{\partial t} = -\boldsymbol{v}\cdot\nabla\boldsymbol{v} + (\boldsymbol{J}\times\boldsymbol{B} - \nabla p)/\rho + \nabla\cdot\left[\nu(\boldsymbol{v}-\boldsymbol{v}_0)\right], \tag{3}$$

$$\frac{\partial \boldsymbol{B}}{\partial t} = -\nabla\times\boldsymbol{E}, \tag{4}$$

$$\boldsymbol{E} = -\boldsymbol{v}\times\boldsymbol{B} + \eta(\boldsymbol{J}-\boldsymbol{J}_0), \tag{5}$$

$$\boldsymbol{J} = \nabla\times\boldsymbol{B}, \tag{6}$$

where ρ, p, $\boldsymbol{v}$, $\boldsymbol{B}$, $\boldsymbol{E}$, and $\boldsymbol{J}$ are the plasma density, plasma pressure, plasma velocity, magnetic field, electric field, and current density, respectively. Variables with the subscript '0' represent the initial equilibrium quantities. $\Gamma = 5/3$ is the ratio of the specific heat of the plasma. The variables are normalized as follows: $\boldsymbol{x}/a \to \boldsymbol{x}$, $\rho/\rho_{00} \to \rho$, $p/\left(B_{00}^2/\mu_0\right) \to p$, $\boldsymbol{v}/v_{\rm A} \to \boldsymbol{v}$, $t/\tau_{\rm A} \to t$, $\boldsymbol{J}/(B_{00}/\mu_0 a) \to \boldsymbol{J}$, $\boldsymbol{B}/B_{00} \to \boldsymbol{B}$, and $\boldsymbol{E}/(v_{\rm A}B_{00}) \to \boldsymbol{E}$, where a is the minor radius, $v_{\rm A} = B_{00}/\sqrt{\mu_0\rho_{00}}$ is the Alfven speed, and $\tau_{\rm A} = a/v_{\rm A}$ is the Alfven time. In addition, ρ_{00} and B_{00} are the initial plasma density and magnetic field at the magnetic axis, respectively. The plasma diffusion coefficient D, thermal conductivities $\kappa_\parallel$ and $\kappa_\perp$, viscosity ν, and resistivity η are normalized as follows: $D/\left(a^2/\tau_{\rm A}\right) \to D$, $\kappa_\parallel/\left(a^2/\tau_{\rm A}\right) \to \kappa_\parallel$, $\kappa_\perp/\left(a^2/\tau_{\rm A}\right) \to \kappa_\perp$, $\nu/\left(a^2/\tau_{\rm A}\right) \to \nu$ and $\eta/\left(\mu_0 a^2/\tau_{\rm A}\right) \to \eta$.

When solving Eqs. (1)–(6), the spatial derivatives are calculated by the fourth-order central difference scheme, and the time integration is carried out with the fourth-order Runge–Kutta scheme. Since the physical boundary is not located on the rectangular grids in the x–z plane, the cut-cell[47] method is adopted to solve boundary conditions.

3. Simulation results

3.1. Simulation set-up

In all the simulations in the present paper, a toroidal tokamak configuration with an aspect ratio $R_0/a = 4/1$ is adopted. The initial profiles of the safety factor and the plasma pressure used in this subsection are shown in Fig. 1, and their formulas are provided in Eqs. (7) and (8), respectively,

$$q = q_0 \times \left(1 + \left(\frac{\psi_{\rm n}}{q_1}\right)^{\alpha}\right)^{1/\alpha}, \tag{7}$$

$$p = p_0 \times (b \times {\rm e}^{-\psi_{\rm n}/0.1} + (1-b)\times(1-\psi_{\rm n})), \tag{8}$$

where $\psi_{\rm n}$ is the normalized poloidal flux, $q_0 = 2.01$ is the safety factor value on the magnetic axis, $q_{\rm e} = 3.1$ is the safety factor at the plasma boundary, $\alpha = 4.0$ is a parameter to determine the magnetic shear in the central region and $q_1 = \left[(q_{\rm e}/q_0)^{\alpha} - 1\right]^{-1/\alpha}$. For pressure profiles, $p_0 = 2.21\%$ is the plasma pressure on the magnetic axis, and $b = 0.9$ is chosen to control the pressure gradient. With such parameters, the safety factor profile is flat and close to 2.0, and the pressure gradient is sufficiently large. It is a typical equilibrium for infernal modes in hybrid tokamak scenarios and is calculated by the Q-solver[48] code. To avoid excitation of the 2/1 tearing mode while keeping the physics of the infernal mode unchanged, all cases are chosen with q_0 slightly above 2. Uniform meshes with 256×64×256 grids in (R, ϕ, Z) are used in all the simulations. Since the infernal modes are internal modes, we fix all the perturbed variables to be zero at the last closed surface for the sake of numerical stability. Random perturbations are applied for a few time steps at the beginning of all the simulations.

3.2. Linear results

In this subsection, we focus on the linear properties of infernal modes. The diffusion parameters in Eqs. (1)–(5) are fixed to be $\kappa_\parallel = 1.0$, $D = 1\times10^{-7}$, $\kappa_\perp = 1\times10^{-7}$, $\nu = 1\times10^{-7}$, and $\eta = 1\times10^{-6}$, respectively, unless otherwise stated. D, $\kappa_\perp$, and ν are smaller than η by one order of magnitude so that they hardly influence the linear growth rates of the modes. Even though there is no $q = 2$ resonant surface, the equilibrium shown in Fig. 1 is unstable. The evolution of the perturbed kinetic energy is shown in Fig. 2(a), indicating that the toroidal mode number of the dominant component is $n = 1$. The evolution of the perturbed toroidal electric field is shown in Fig. 2(b), and it implies that a series of components with $n = 1$ but different m couple together since all the components have the same growth rate. The radial profiles of the perturbed electric field for all mode components are shown in

Fig. 2(c). Among them, the amplitude of the $m/n = 2/1$ component is the largest, which is attributed to the safety factor being close to 2.0 in the central region. The 3/1 mode exhibits an oscillatory behavior, with its amplitude forming a bimodal structure. In addition, other components are also present in this region due to toroidal coupling effects.[37,49,50] This is the distinctive characteristic of infernal modes. In contrast, for quasi-interchange modes, the 1/1, 2/2, 3/3, and 4/4 modes develop independently.[11] These components together lead to a 2D distribution of the perturbed pressure shown in Fig. 2(d). Such patterns are mainly determined by the 2/1 component and modified by other components.

As discussed in previous studies, the pressure gradient is the dominant factor for infernal modes.[13,39] As a result, there exists a pressure threshold for the infernal mode to be unstable. For the q and pressure profiles given in Subsection 3.1, the pressure threshold is about $p_0 = 2.2\%$. Below this threshold, the system is stable. Just above the threshold (*e.g.*, $p_0 = 2.21\%$), the system is marginally unstable, and resistivity becomes important. The linear growth rate of the mode obeys $\gamma \sim \eta^{3/13}$. However, when the plasma pressure far exceeds this threshold (*e.g.*, $p_0 = 3.01\%$), the system is almost ideally unstable and the linear growth rate will become independent of η. The linear growth rates of the infernal modes with $p_0 = 2.21\%$ and $p_0 = 3.01\%$ *versus* different η are shown in Figs. 3(a) and 3(b). These results are consistent with previous theoretical or numerical investigations.

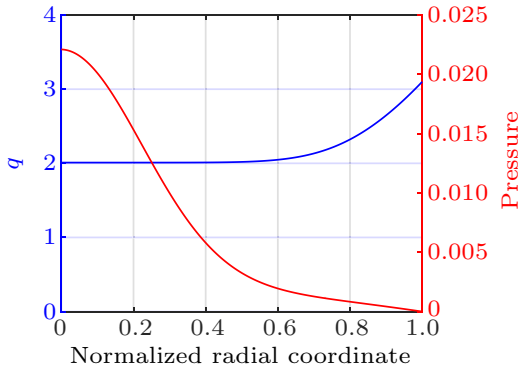


Fig. 1. Initial profiles of the safety factor and the plasma pressure used in the simulations.

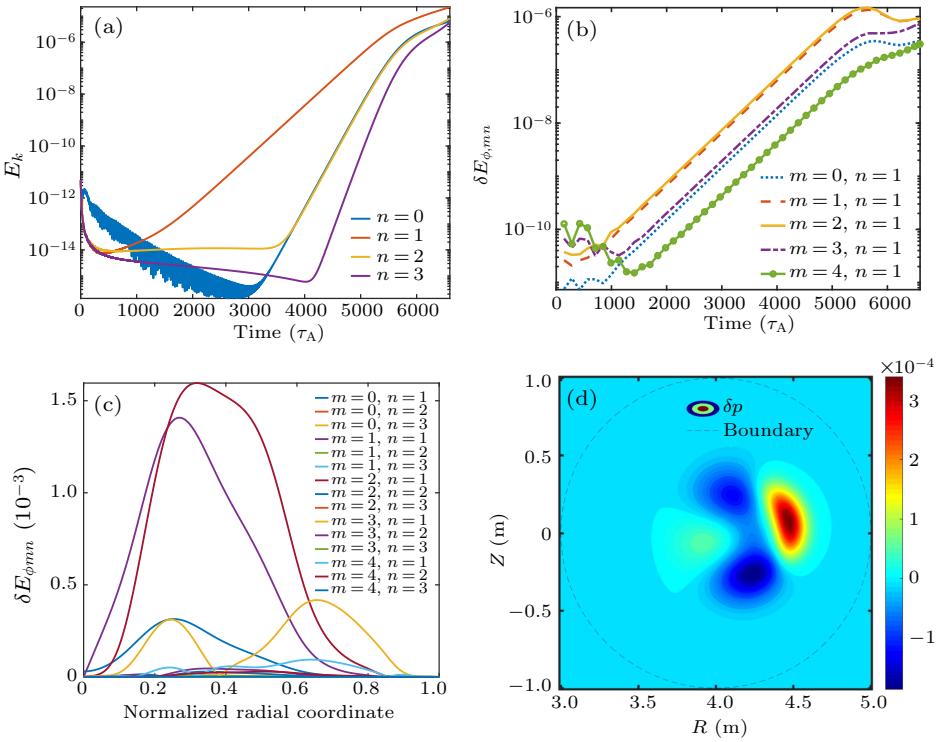


Fig. 2. (a) Evolution of the perturbed kinetic energy E_k for components with different n. (b) Evolution of the perturbed toroidal electric field for the components with $n = 1$ and different m. (c) Radial profiles of the amplitudes of the perturbed toroidal electric field in the linear phase. (d) 2D distributions of the perturbed pressure in the linear phase.

As shown in Fig. 3(a), the resistive scaling in the low- and high-resistivity regions exhibits slight differences. This behavior can be understood from the growth rate dispersion relation of the infernal mode, $\gamma^{5/4}(\gamma^2 - \gamma_{\rm ideal}^2) = \gamma_{\rm res}^{13/4}$, where $\gamma_{\rm ideal}$ is the growth rate in ideal MHD and $\gamma_{\rm res}$ is the resistive growth rate at the stability boundary ($\gamma_{\rm ideal} = 0$), with $\gamma_{\rm res} \propto \eta^{3/13}$. In low-resistivity conditions, $\gamma_{\rm ideal}$ dominates, while in high-resistivity conditions, $\gamma_{\rm res}$ is more significant, making the growth rate more sensitive to resistivity. The relative contributions of $\gamma_{\rm ideal}$ and $\gamma_{\rm res}$ explain why the infernal mode exhibits different resistive scaling behaviors at different pressures, consistent with previous theoretical and numerical studies.[13,39]

For the infernal mode to be unstable, the minimum safety factor $q_{\rm min}$ needs to be close to 2.0. As shown in Fig. 4, increasing $q_{\rm min}$ from 2.0 to 2.09 gradually reduces the linear

growth rate to zero, consistent with previous studies that identify $q_{\min} \approx 2$ as critical for destabilization. This behavior arises from the stabilizing effect of magnetic field line bending: the perturbed perpendicular magnetic field induced by plasma displacement generates a restoring force that resists deformation. The farther $q_{\min}$ is from 2, the stronger this stabilization, leading to a lower growth rate. Note that the growth rate is not strictly inversely proportional to $q_{\min}$, but the two quantities are negatively correlated.

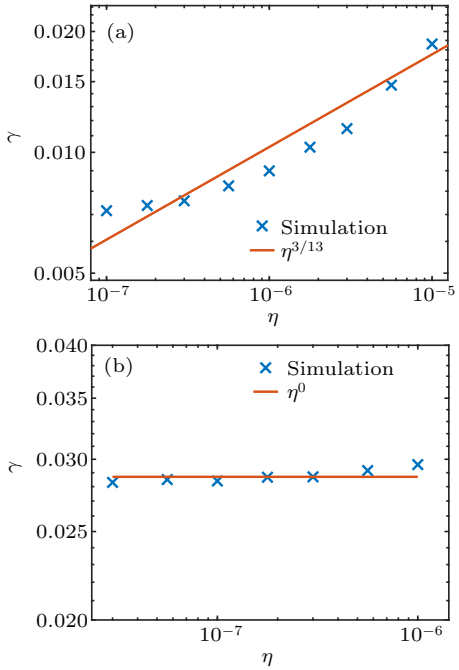


Fig. 3. Linear growth rates of the infernal modes with (a) $p_0 = 2.21\%$ and (b) $p_0 = 3.01\%$ *versus* different η. D, $\kappa_\perp$, and ν are kept at one-tenth of η so that other diffusion parameters hardly influence the linear growth rates in these simulations.

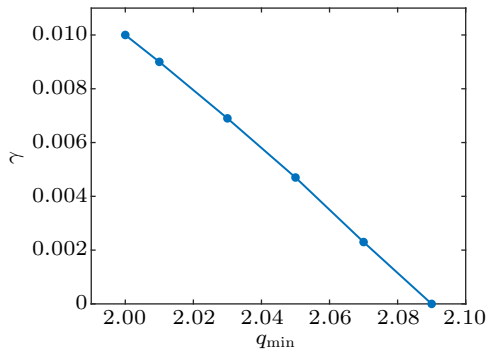


Fig. 4. The growth rate of the infernal mode for cases with different $q_{\min}$.

3.3. Nonlinear phase — explosive growth

Subsection 3.1 focuses on the linear properties of the infernal modes, and this subsection focuses on their nonlinear evolution. Since the infernal modes with the initial equilibrium in Fig. 1 sometimes experience explosive growth in the nonlinear phase and tend to be numerically unstable, the diffusion parameters are chosen to be larger than those used in Subsection 3.1, *i.e.*, $D = 1 \times 10^{-6}$, $\kappa_\perp = 1 \times 10^{-6}$, $\nu = 1 \times 10^{-5}$, $\eta = 1 \times 10^{-6}$, and $\kappa_\parallel = 0.1$.

The evolutions of the perturbed kinetic energy and its growth rate are shown in Figs. 5(a) and 5(b), respectively. One notable characteristic is that the mode experiences explosive growth in the nonlinear phase. Although infernal modes have very large linear growth rates (for this case, $\gamma \sim 0.0085$) and weakly depend on plasma resistivity, the nonlinearly explosive growth indicates that infernal modes will be even more dangerous than those expected by linear analysis.

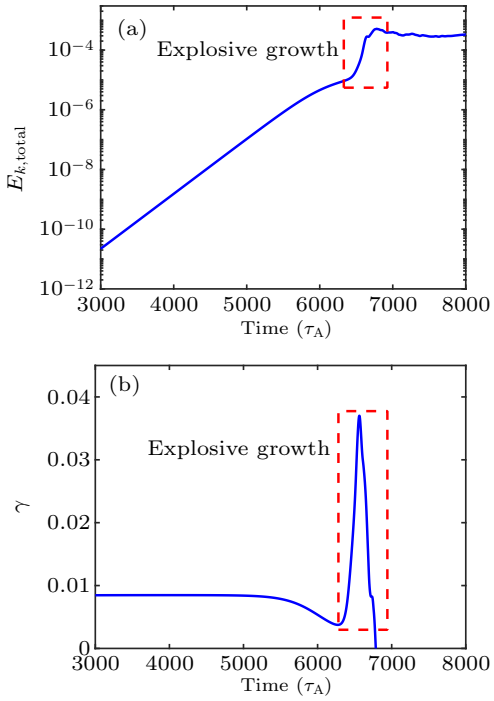


Fig. 5. Evolutions of (a) the total kinetic energy and (b) the growth rate with $\kappa_\parallel = 0.1$.

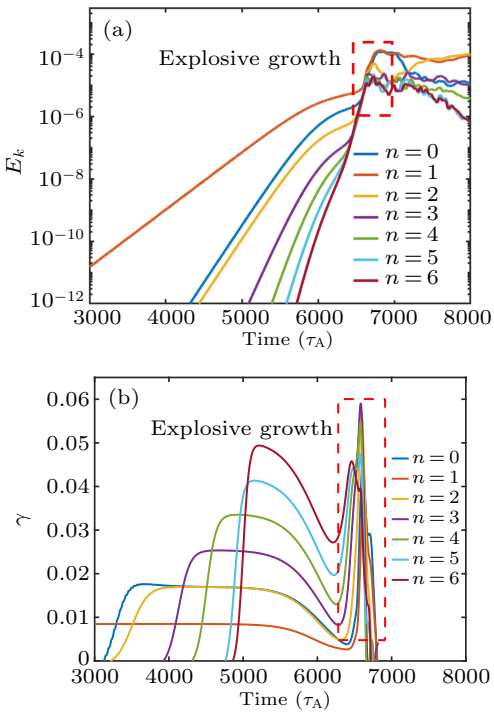


Fig. 6. Evolutions of (a) the kinetic energy and (b) the growth rate with different toroidal mode numbers and $\kappa_\parallel = 0.1$.

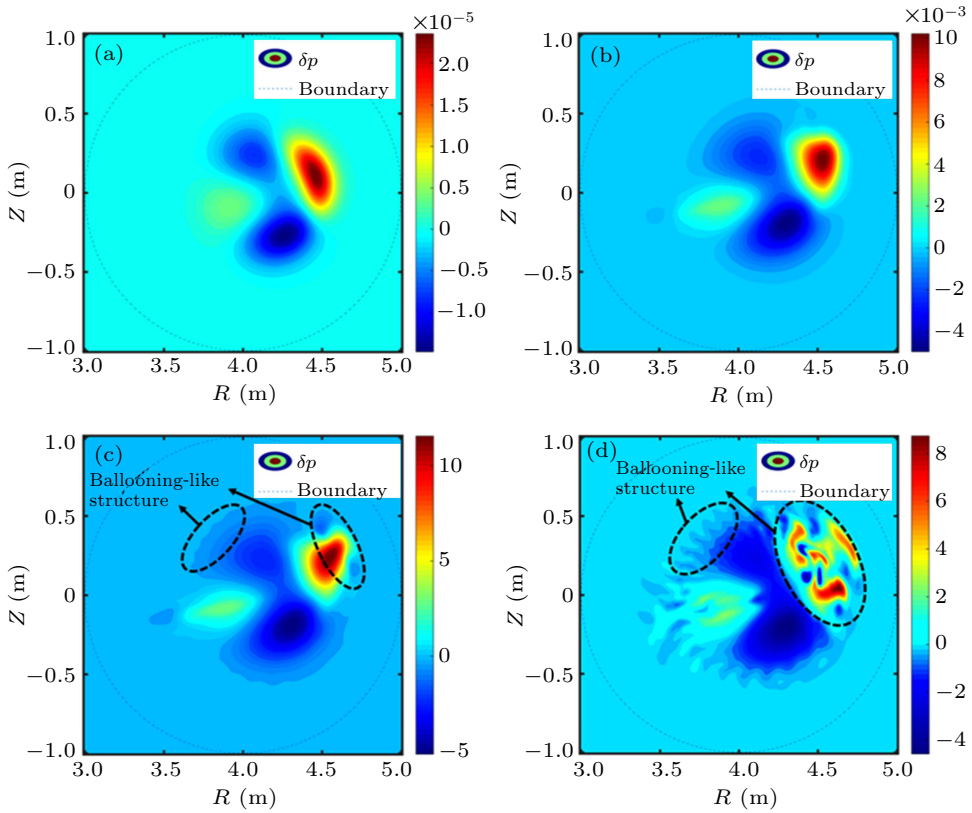


Fig. 7. Contour plots of pressure perturbation at four typical moments: (a) $t = 3254\tau_A$, (b) $t = 6366\tau_A$, (c) $t = 6508\tau_A$, (d) $t = 6649\tau_A$ ($\kappa_\parallel = 0.1$).

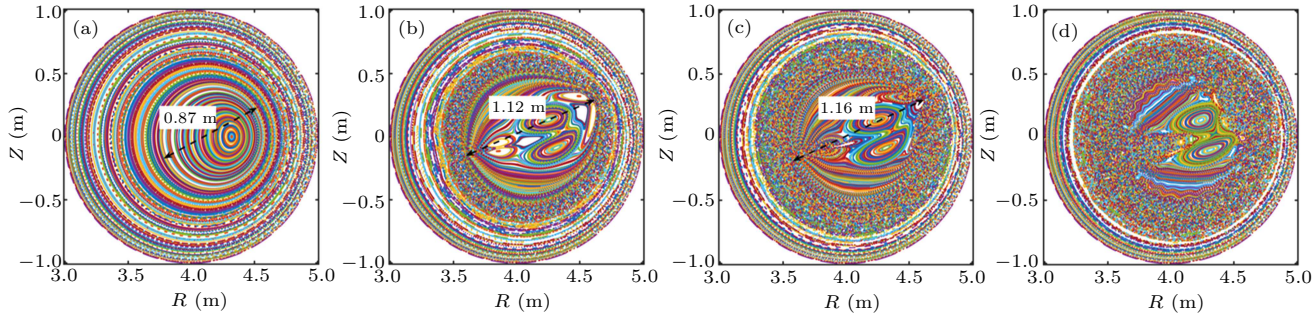


Fig. 8. Poincare plots of magnetic field lines at four typical moments: (a) $t = 3254\tau_A$, (b) $t = 6366\tau_A$, (c) $t = 6508\tau_A$, (d) $t = 6649\tau_A$ ($\kappa_\parallel = 0.1$).

Through the Fourier transform method, we also know the contribution made by each component. The evolutions of the kinetic energy for components with different n and their growth rates are shown in Figs. 6(a) and 6(b), respectively. For the $n = 1$ component, it dominates the linear phase and the peak value of the nonlinear growth rate is 0.038 (more than 4 times its linear growth rate). High-n components are almost negligible in the linear phase since their amplitudes are several orders of magnitude smaller than the $n = 1$ component. They are beat modes of the $n = 1$ component before $t \sim 6000\tau_A$ because the growth rates $\gamma_n = n\gamma_{n=1}$. When the infernal modes enter the nonlinear phase ($t \sim 6000\tau_A$ to $7000\tau_A$), the amplitudes of the high-n components are comparable to the $n = 1$ component but have larger growth rates. For the $n = 6$ component, its maximum growth rate can be as large as $\gamma_6 = 0.059$, which is 7 times larger than the linear growth rate of the infernal mode.

The 2D distributions of the perturbed plasma pressure at four typical moments are shown in Fig. 7. In the linear phase, the patterns of the perturbed pressure are dominated by the 2/1 component and coupled with 1/1, 3/1, and 4/1 components (Figs. 7(a) and 7(b)). However, as shown in Figs. 7(c) and 7(d), 'ballooning-like' structures are formed during the explosive growth phase. It is evident that the high-n components are crucial for the explosive growth of the infernal mode.

The formation of 'ballooning-like' structures is related to the magnetic flux surface destruction and the local large pressure gradient. Such a process can be seen from the Poincare plots of the magnetic field lines (Fig. 8) and the 2D distributions of the total plasma pressure (Fig. 9) at the same moments as in Fig. 7. Initially, the central region exhibits high pressure and low but finite magnetic shear (Figs. 8(a) and 9(a)). The diameter of this large pressure region is about 0.87. During

the infernal mode development, especially for the 2/1 component, the high-pressure region is elongated in one direction and squeezed in another direction (Figs. 8(b), 8(c), 9(b), and 9(c)). The major axis of the high-pressure region increases to 1.25 (Fig. 9(d)). As the high-pressure region stretches, the surrounding magnetic field becomes stochastic (Figs. 8(b)–8(d)). However, due to the low parallel thermal conductivity, parallel plasma diffusion is very slow, and the pressure profile does not flatten in this region. Instead, a steep pressure gradient forms within the stochastic region. This localized steep pressure gradient causes ideal-MHD instabilities (probably the interchange instability). This explains the rapid growth of high-n modes and the occurrence of explosive behavior in the nonlinear phase.

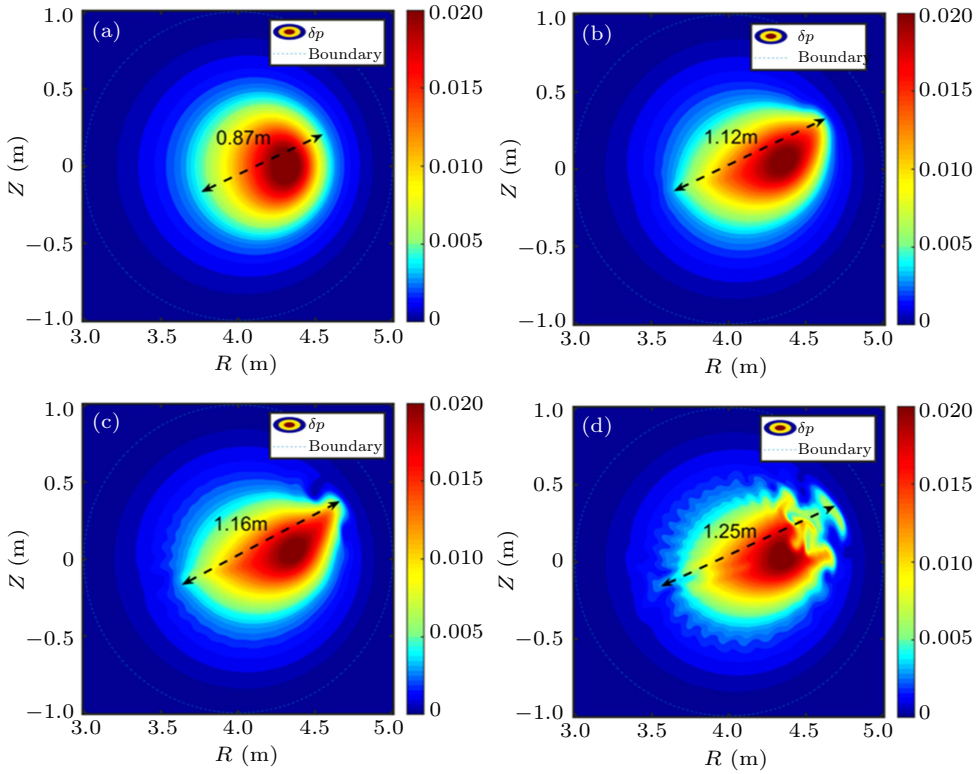


Fig. 9. Contour plots of plasma pressure at four typical moments: (a) $t = 3254\tau_A$, (b) $t = 6366\tau_A$, (c) $t = 6508\tau_A$, (d) $t = 6649\tau_A$ ($\kappa_\parallel = 0.1$).

3.4. Nonlinear phase — saturation

Subsection 3.3 presents a case where infernal modes experience explosive growth in the nonlinear phase. In fact, the nonlinear behaviors of infernal modes can follow two distinct paths: either explosive growth or saturation. In this subsection, a case with nonlinear saturation of the infernal mode is presented, along with a discussion on the physical mechanisms underlying the transition between these two nonlinear regimes.

The evolutions of the kinetic energy and the growth rate with different toroidal mode numbers and $\kappa_\parallel = 1$ are shown in Fig. 10. The only difference between the simulations in Figs. 10 and 6 is that the parallel thermal conductivity $\kappa_\parallel$ is 1.0, which is 10 times larger than that in Fig. 6. In this case, there is no explosive growth in the nonlinear phase, and the infernal mode eventually saturates. The $m/n = 2/1$ component dominates in both linear and nonlinear phases, and the amplitudes of the high-n components are much smaller than the $n = 1$ component. The maximum kinetic energy of the explosive-growth infernal mode in Fig. 6 is 1.2×10^{-4}, and the final value for the saturation case is 1.3×10^{-5}, which is about one order of magnitude smaller.

The 2D distributions of the perturbed and total pressure, and the Poincare plots of the magnetic field lines at the beginning of the nonlinear phase ($t = 5659\tau_A$) and the final saturation stage ($t = 11224\tau_A$) are shown in Fig. 11. Similar to the explosive growth cases, the 2/1 component leads to an elongated high-pressure region. However, in the saturation cases, the magnetic field lines surrounding the high-pressure region do not become stochastic. The large parallel thermal conductivity helps to diffuse the plasma pressure and suppress the high-n modes. As a result, no "ballooning-like" structures form in the saturation cases. Since the mode's amplitude is much smaller, the major axis of the high-pressure region is only 1.12 and much smaller than that in the explosive growth case.

Figures 6 and 10 imply that the parallel thermal conductivity ($\kappa_\parallel$) is a crucial parameter for the nonlinear behaviors of the infernal mode. As a result, we scan $\kappa_\parallel$ to investigate its influence on infernal modes. The evolutions of the kinetic energy and growth rate for the cases with $\kappa_\parallel = 0.1$, $\kappa_\parallel = 0.3$, $\kappa_\parallel = 0.5$, $\kappa_\parallel = 1.0$, and $\kappa_\parallel = 3.0$ are shown in Fig. 12. It is evident that $\kappa_\parallel$ has little impact on the linear growth rate of

the mode. However, when $\kappa_\parallel$ is larger than a threshold value (typically $\kappa_\parallel >\sim 0.3$), the parallel diffusion of the pressure perturbation is fast and the nonlinear growth of high-n modes is suppressed. As a result, the nonlinearly explosive growth disappears, and the infernal mode finally saturates.

Thermal conductivity $\kappa_\parallel$ is not the only parameter that affects the nonlinear evolution regimes of the infernal modes. The nonlinear behaviors of the infernal modes will also be influenced by viscosity since high viscosity can suppress high-n modes. The evolutions of the kinetic energy and the normalized growth rate of the cases with $\kappa_\parallel = 0.3$ but different ν are shown in Fig. 13. In Fig. 13(b), we have normalized the values of the growth rates to their linear values to show the growth rate change in the nonlinear phase. The peak value of the nonlinear growth rate decreases with increasing viscosity, *i.e.*, the explosive growth is weaker and weaker. The infernal modes tend to saturate with large viscosities.

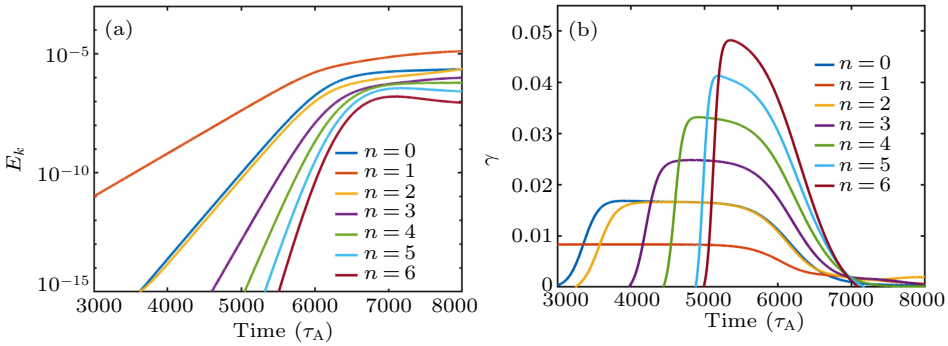


Fig. 10. Evolutions of (a) the kinetic energy and (b) the growth rate with different toroidal mode numbers and $\kappa_\parallel = 1$.

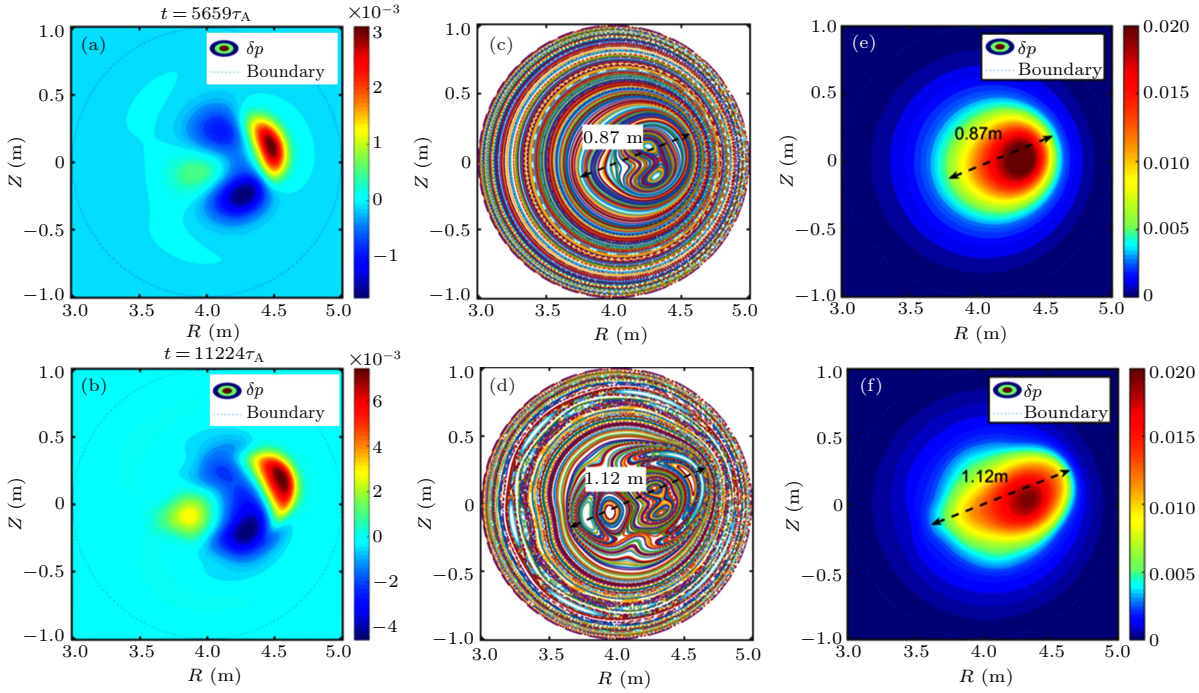


Fig. 11. The 2D distributions of the perturbed pressure, the Poincare plots of the magnetic field lines, and the total pressure at the beginning of the nonlinear phase ($t = 5659\tau_A$) and the final saturation stage ($t = 11224\tau_A$) with $\kappa_\parallel = 1$.

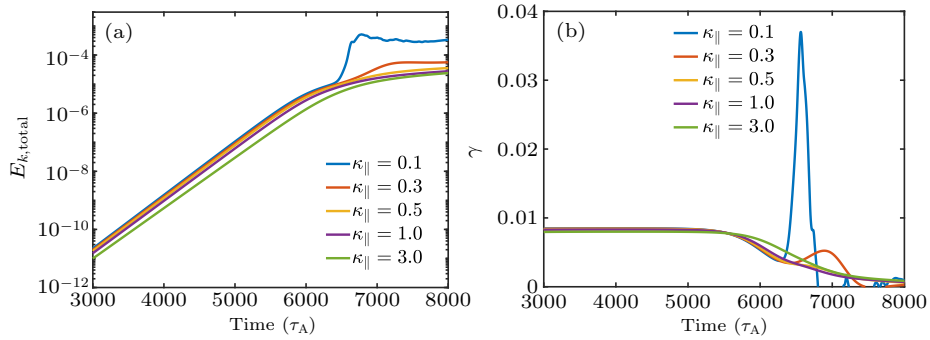


Fig. 12. Evolutions of (a) the total kinetic energy and (b) the growth rates with different parallel thermal conductivities.

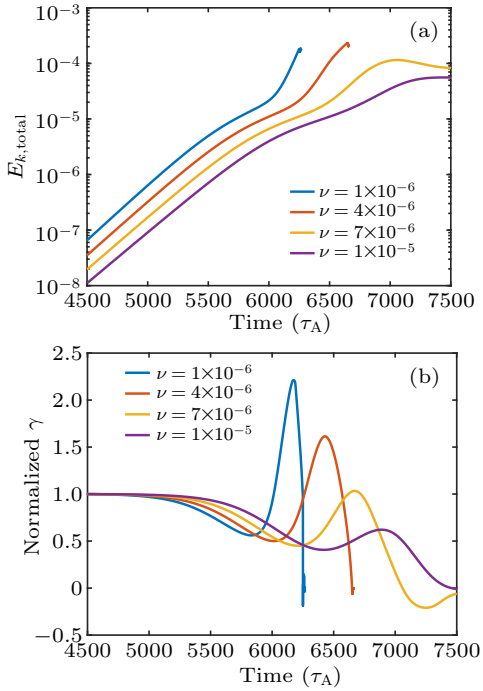


Fig. 13. Evolutions of (a) the total kinetic energy and (b) the normalized growth rates with $\kappa_\parallel = 0.3$ and different ν.

To illustrate the distinct nonlinear evolution regimes of the infernal modes, simulations with $\kappa_\parallel$ (0.1–3.0) and ν (1×10^{-6}–1×10^{-5}) are presented. Table 1 presents the linear growth rate γ_{lin} and peak nonlinear growth rate γ_{non} with different $\kappa_\parallel$ and ν. In several cases, there is no peak growth rate at all, and γ_{non} is defined as 'NaN'. The nonlinear behaviors of the infernal modes with different $\kappa_\parallel$ and ν are shown in Fig. 14. Since the explosive growth requires that the maximum nonlinear growth rate is larger than its linear growth rate, the cases with $\gamma_{\mathrm{non}} < \gamma_{\mathrm{lin}}$ or the $\gamma_{\mathrm{non}} = \mathrm{NaN}$ are marked as 'w/o explosive growth'. Figure 14 clearly indicates the distinct nonlinear evolution regimes of the nonlinear phases of the infernal modes and the importance of the large parallel diffusion.

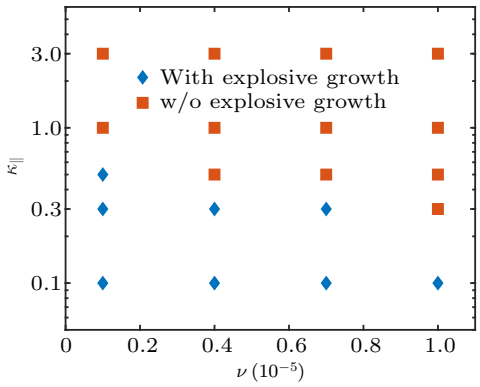


Fig. 14. Nonlinear behaviors of the infernal modes with different ν and $\kappa_\parallel$. The blue diamond marks indicate cases with explosive growth and the red square marks indicate cases without explosive growth.

Table 1. Linear growth rate γ_{lin} and the peak value of the nonlinear growth rate γ_{non} with different $\kappa_\parallel$ and ν. 'NaN' indicates that there is no peak value in the nonlinear phase of the infernal mode.

$(\gamma_{\mathrm{lin}}/\gamma_{\mathrm{non}})\times10^3$	$\nu = 1\times10^{-6}$	$\nu = 4\times10^{-6}$	$\nu = 7\times10^{-6}$	$\nu = 1\times10^{-5}$
$\kappa_\parallel = 0.1$	8.8/20.2	9.0/48.0	8.7/38.7	8.5/36.8
$\kappa_\parallel = 0.3$	9.2/20.2	8.9/14.3	8.7/8.8	8.4/5.2
$\kappa_\parallel = 0.5$	9.2/11.9	8.9/6.4	8.6/NaN	8.4/NaN
$\kappa_\parallel = 1.0$	9.1/5.3	8.8/NaN	8.5/NaN	8.3/NaN
$\kappa_\parallel = 3.0$	8.8/NaN	8.6/NaN	8.3/NaN	8.0/NaN

4. Summary

This paper numerically investigated the linear and nonlinear evolution of infernal modes with a flat q profile and high plasma pressure in the central region, which is close to the hybrid tokamak scenarios. Although a rational surface is not necessary for infernal modes, they still require that the flat q profile be not far away from a rational surface. For equilibria with $q_{\mathrm{min}} \approx 2.0$, the dominating unstable mode is $m/n = 2/1$ and is coupled with other components with the same n but different m. The development of the infernal modes then leads to an elongated high-pressure region.

Plasma pressure is also crucial for infernal modes. For cases with high plasma pressure, the system is almost unstable to ideal-MHD instability and the linear growth rates are independent of plasma resistivity. However, if the pressure is just above the unstable threshold, the linear growth rates depend on plasma resistivity, and the scaling law for the infernal modes is $\gamma \sim \eta^{3/13}$.

The nonlinear behaviors of the infernal modes exhibit distinct evolution regimes. In certain cases, the infernal modes experience explosive growth during the nonlinear phase, while in others, the growth remains moderate. The explosive nonlinear growth is attributed to an interchange instability, which occurs when the magnetic field lines become stochastic and the local pressure gradient is sufficiently large. The patterns of the perturbed pressure are ballooning-like, and the dominant toroidal mode numbers are greater than 1.

The nonlinear evolution of infernal modes is strongly influenced by parallel thermal conductivity. An accurate treatment of parallel transport in nonlinear simulations is essential, as it determines whether the mode undergoes explosive growth or saturates. When the parallel conductivity exceeds a threshold, diffusion along magnetic field lines is fast enough to suppress interchange-like instabilities, leading to saturation. Viscosity also affects explosive growth, particularly for high-n

modes. A 2D parameter map delineates the transition between explosive and saturated regimes, providing guidance for simulation studies and informing tokamak operation and stability control strategies.

Acknowledgements

Project supported by the National Magnetic Confinement Fusion Program of China (Grant No. 2019YFE03090200) and the National Natural Science Foundation of China (Grant Nos. 12375224, 11975231, 12005185, 11835010, and 12175277).

References

[1] Staebler A, Sips A, Brambilla M, Bilato R, Dux R, Gruber O, Hobirk J, Horton L, Maggi C and Manini A 2005 *Nucl. Fusion* **45** 617
[2] Gormezano C, Sips A C C, Luce T C, *et al*. 2007 *Nucl. Fusion* **47** S285
[3] von Goeler S, Stodiek W and Sauthoff N 1974 *Phys. Rev. Lett.* **33** 1201
[4] Sauter O, Westerhof E, Mayoral M L, *et al*. 2002 *Phys. Rev. Lett.* **88** 105001
[5] Buttery R J, Hender T C, Howell D F, Haye R J L, Parris S, Sauter O, Windsor C G and Contributors J E 2004 *Nucl. Fusion* **44** 678
[6] Wang H Y, Jiang S, Liu T, Wei L, Luan Q B and Wang Z X 2024 *Chin. Phys. B* **33** 065202
[7] Wesson J A 1986 *Plasma Phys. Control. Fusion* **28** 243
[8] Aydemir A 1987 *Phys. Rev. Lett.* **59** 649
[9] Hastie R J and Hender T C 1988 *Nucl. Fusion* **28** 585
[10] Waelbroeck F L and Hazeltine R D 1988 *The Physics of Fluids* **31** 1217
[11] Zhang W, Ma Z, Wang X and Chen W 2022 *Phys. Plasmas* **29** 102509
[12] Manickam J, Pomphrey N and Todd A M M 1987 *Nucl. Fusion* **27** 1461
[13] Charlton L A, Carreras B A and Lynch V E 1990 *Physics of Fluids B: Plasma Physics* **2** 1574
[14] Jardin S C, Munaretto S, Ferraro N M, Kaye S M, Kleiner A and Lyons B C 2024 *Phys. Plasmas* **31** 032503
[15] Charlton L, Baylor L, Edwards A, Hammett G, Houlberg W, Kupschus P, Lynch V, Milora S, O'Rourke J and Schmidt G 1991 *Nucl. Fusion* **31** 1835
[16] Buratti P, Baruzzo M, Buttery R J, Challis C D, Chapman I T, Crisanti F, Figini L, Gryaznevich M, Hender T C, Howell D F, Han H, Imbeaux F, Joffrin E, Hobirk J, Kwon O J, Litaudon X, Mailloux J and contributors J E 2012 *Nucl. Fusion* **52** 023006
[17] Menard J E, Bell R E, Fredrickson E D, Gates D A, Kaye S M, LeBlanc B P, Maingi R, Medley S S, Park W, Sabbagh S A, Sontag A, Stutman D, Tritz K, Zhu W and the N R T 2005 *Nucl. Fusion* **45** 539
[18] Stutman D, Delgado-Aparicio L, Gorelenkov N, Finkenthal M, Fredrickson E, Kaye S, Mazzucato E and Tritz K 2009 *Phys. Rev. Lett.* **102** 115002
[19] Chapman I T, Hua M D, Pinches S D, Akers R J, Field A R, Graves J P, Hastie R J, Michael C A and the MAST Team 2010 *Nucl. Fusion* **50** 045007
[20] Deng W, Liu Y, Wang X Q, Chen W, Dong Y B, Ohdachi S, Ji X Q, Shen Y, Cao J Y, Zhou J, Feng B B, Li Y G, Huang X L, Gao J M, Han X Y, Huang M and Wang X G 2014 *Nucl. Fusion* **54** 013010
[21] Yu L M, Chen W, Jiang M, *et al*. 2017 *Nucl. Fusion* **57** 036023
[22] Wu J, Lan T, Ding W X, *et al*. 2021 *Nucl. Fusion* **61** 066003
[23] Zhang J, Zhang Y, Chen W, *et al*. 2023 *Nucl. Fusion* **63** 086014
[24] Zhang R B, Wang X Q, Xiao C J, Wang X G, Liu Y, Deng W, Chen W, Ding X T, Duan X R and the HL-2 A Team 2014 *Plasma Phys. Control. Fusion* **56** 095007
[25] Shi P W, Zhu X L, Liang A S, Chen W, Shi Z B, Wang T B, Yang Z C, Yu L M, Jiang M, He X X, Bai X Y, Ji X Q, Zhong W L, Xu M, Wang Z X and Duan X R 2022 *Nucl. Fusion* **62** 106009
[26] Ichiguchi K, Suzuki Y, Todo Y, Sakakibara S, Ida K, Takemura Y, Sato M, Sugiyama L E and Carreras B A 2021 *Nucl. Fusion* **61** 126056
[27] Günter S, Schade S, Maraschek M, Pinches S D, Strumberger E, Wolf R, Yu Q and Team A U 2000 *Nucl. Fusion* **40** 1541
[28] Yuan Y, Hu L, Xu L, Chao Y, Liu H, Li Y, Zhang T, Hao B, Chen K, Zhang J, Duan Y, Lin S, Mao S and Team E 2020 *Nucl. Fusion* **60** 016003
[29] Xu M, Ma R, Xu L, *et al*. 2022 *Nucl. Fusion* **62** 126041
[30] Hua M D, Chapman I T, Pinches S D, Hastie R J and Team T M 2010 *Europhys. Lett.* **90** 55001
[31] Marchenko V S 2014 *Phys. Plasmas* **21** 054504
[32] Wan Y, Li J, Liu Y, *et al*. 2017 *Nucl. Fusion* **57** 102009
[33] Nakamura Y, Ishizawa A and Ishida Y 2020 *Phys. Plasmas* **27** 092509
[34] Ozeki T, Azumi M, Tokuda S and Ishida S 1993 *Nucl. Fusion* **33** 1025
[35] Breslau J A, Chance M S, Chen J, Fu G Y, Gerhardt S, Gorelenkov N, Jardin S C and Manickam J 2011 *Nucl. Fusion* **51** 063027
[36] Jardin S C, Ferraro N M, Guttenfelder W, Kaye S M and Munaretto S 2022 *Phys. Rev. Lett.* **128** 245001
[37] Brunetti D, Graves J P, Halpern F D, Luciani J F, Lütjens H and Cooper W A 2015 *Plasma Phys. Control. Fusion* **57** 054002
[38] Ham C, Connor J, Cowley S, Gimblett C, Hastie R, Hender T and Martin T 2012 *Plasma Phys. Control. Fusion* **54** 025009
[39] Charlton L A, Hastie R J and Hender T C 1989 *Physics of Fluids B: Plasma Physics* **1** 798
[40] Brunetti D, Graves J P, Cooper W A and Wahlberg C 2014 *Plasma Phys. Control. Fusion* **56** 075025
[41] Glasser A H, Greene J M and Johnson J L 1975 *The Physics of Fluids* **18** 875
[42] Park W, Fredrickson E D, Janos A, Manickam J and Tang W M 1995 *Phys. Rev. Lett.* **75** 1763
[43] Paley J I, Andrew P, Cowley S C, Fundamenski W, Huber A and Contributors J E 2005 *J. Nucl. Mater.* **337–339** 702
[44] Lütjens H and Luciani J F 1997 *Phys. Plasmas* **4** 4192
[45] Myers S A, Dudson B D and Wilson H R 2013 *Plasma Physics and Controlled Fusion* **55** 125016
[46] Zhang W, Jardin S C, Ma Z W, Kleiner A and Zhang H W 2021 *Comput. Phys. Commun.* **269** 108134
[47] Duan L, Wang X and Zhong X 2010 *J. Comput. Phys.* **229** 7207
[48] DeLucia J, Jardin S C and Todd A M M 1980 *J. Comput. Phys.* **37** 183
[49] Leboeuf J N, Lynch V E and Carreras B A 2001 *Phys. Plasmas* **8** 3358
[50] Coste-Sarguet M and Graves J P 2024 *Plasma Phys. Control. Fusion* **66** 095004